Transactions on Engineering and Computing Sciences - Vol. 11, No. 4
Publication Date: August 25, 2023
DOI:10.14738/tecs.114.15392.
Alvarez, R. & Camacho, M. (2023). Applying High-Resolution Gravity Analysis to Volcanic Plumbing Systems: The Case of Nevado De Toluca Volcano, Mexico. Transactions on Engineering and Computing Sciences, 11(4). 184-207.



Applying High-Resolution Gravity Analysis to Volcanic Plumbing Systems: The Case of Nevado De Toluca Volcano, Mexico

R. Alvarez
Instituto de Investigaciones en
Matemáticas Aplicadas y en Sistemas (IIMAS),
Universidad Nacional Autónoma de México

M. Camacho
Posgrado en Ciencias de la Tierra,
Universidad Nacional Autónoma de México

ABSTRACT

The plumbing systems of volcanoes are the reservoirs and conduits in which magma is stored and transported in a volcanic structure; their geometries and volumes help place physical limits to the location and size of shallow magma deposits and associated volcanic products. Density variations in the volcanic interior are reflected in the surface gravity field. Performing 3D inversions of the Bouguer anomaly allows the modeling of density distributions, thereby inferring the plumbing system. The process is here exemplified by Nevado de Toluca volcano; it has been active over the past 2.6 My through emissions of andesitic lava flows and pyroclastic deposits. The crater was destroyed at least two times, and the latest activity was recorded at 3.3 ka. Using a high-resolution, satellite gravity data set, and a corresponding magnetic field set, also collected via satellite, we performed 3D inversions on the Bouguer anomaly and the magnetic measurements enclosing this volcanic structure, with resolutions of 500 and 1000 m; the results were obtained in the form of density and magnetic susceptibility volumes, with depths reaching 5 km from the surface. The resolution of the gravity data set unveiled hitherto unknown characteristics of the upper sections of the volcano's plumbing system consisting of a magma chamber and at least two conduits reaching the surface; a cross-section through the summit shows the dacitic dome known as El Ombligo, between those conduits. Preliminary estimates of the depth and volume of the magmatic chamber are 5-6 km below the summit and ~16 km^3, respectively. The low-density regions are also associated with the neighboring San Antonio volcano and the Tenango lava flows. Since the high-resolution, satellite gravity data used here were gathered all over continents and numerous islands between ±60º latitudes, this procedure can be applied to almost any volcanic structure within this latitudinal range.

Keywords: Nevado de Toluca, Satellite gravity data, 3D inversions, Volcanic plumbing systems, Trans Mexican Volcanic Belt.

INTRODUCTION

Plumbing systems are identified as the conduits that transport and store magma from the source to the surface (Murcia at al., 2019); they consist of the network that transports magma from its sources in the asthenosphere and the lithosphere, feeding magma chambers through dikes and sills. Our objective is to locate such conduits and chambers by means of high-resolution (~220 m) gravimetric measurements and 3D inversions.

Gravimetric and magnetic determinations and models were used to associate density and magnetic susceptibility anomalies with the structural traits of the volcanic region. Gravimetric studies help determine the characteristics of volcanic fields (Kauahikaua et al., 2000; Camacho et al., 2018; Camacho and Alvarez, 2020; Guevara et al. 2021); and may help identify their plumbing systems (e.g., Alvarez and Yutsis, 2015; Camacho et al. 2018). Magnetic determinations often complement gravity studies (e.g., Guevara et al. 2021). With the models calculated here, we focused on the processes occurring in the upper 5-6 km of the lithosphere. To illustrate the procedure, we performed 3D inversions of gravity and magnetic data on the Nevado de Toluca volcano in central Mexico. The Trans Mexican Volcanic Belt (TMVB) extends in an E-W direction over 1000 km along the central portion of Mexico and includes numerous volcanic edifices of diverse ages, some of which are in various stages of activity (Ferrari et al., 2012). One of these volcanoes is Nevado de Toluca (NT, 4680 m). The active Popocatepetl volcano and NT are situated at equal distances from Mexico City (~70 km). Toluca City is located ~26 km NE from NT. This is a densely populated region which is one of the large industrial centers of Mexico. Some of its current volcanic hazards were evaluated by Aceves-Quezada et al. (2007).

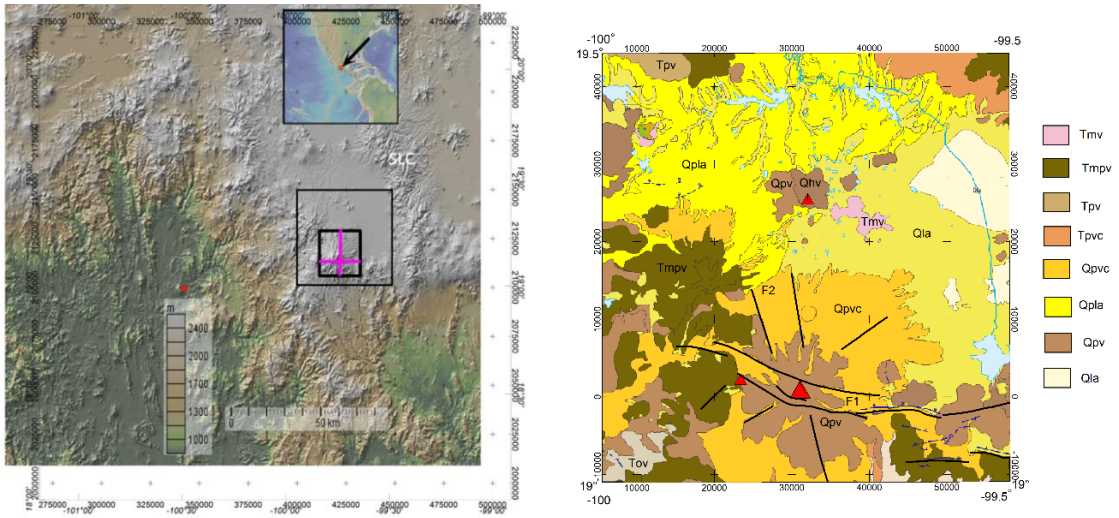
Nevado de Toluca is located at 99º 45'W, 19º 06'N; DeCserna and Fries (1981) obtained an age determination of 1.6 Ma through K-Ar dating for its initial stages of activity. However, Martinez-Serrano et al. (2004) reported that activity started 2.6 Ma with the emission of andesitic lavas, which was modified in the last 40 Ky into emissions of lava flows and pyroclastic deposits with predominantly orthopyroxene–hornblende dacitic compositions, concluding that the construction of the NT volcano occurred at the intersection of three fault systems: the Taxco-Querétaro (NNW-SSE), San Antonio (NE-SW), and Tenango (E-W) fault systems. The authors observed that the Plio-Quaternary E-W trending system actively controlled the ascent and storage of magmas during the recent volcanic activity. Regional fault systems are described in more detail in Norini et al., (2006). Many smaller volcanic structures surround the main edifice (e.g., La Guadalupana, Volcán Gordo, San Antonio volcanoes, as well as the neighboring Tenango volcanic field (Bloomfield, 1974, 1975; Martinez-Serrano et al., 2004) cinder cones and extensive basaltic eruptions conform the landscape.

Cantagrel et al. (1981) reported that NT was built in two very dissimilar phases; the first one lasted over 1 My and the second one developed over the last 100 Ky. However, based on field data and $^{40}Ar/^{39}Ar$ dating, Torres-Orozco et al. (2017) concluded that volcanism at NT was initiated during the mid-Pleistocene (~1.5 Ma). The authors recognized an early history of effusive volcanism with centralized vents, which has been continuous since they found no gaps in the volcano's activity. These authors also recognized that the volcano's original morphology has been severely modified by subsequent explosive eruptions and flank collapses. The original edifice of NT has apparently been destroyed twice, as suggested by debris avalanches, lahars,

and fluvial deposits observed on its south flank (Macías et al., 1997; Capra and Macías, 2000), indicating that the region is prone to explosive activity which could induce major damage in this urban and industrialized area.

Bloomfield and Valastro (1974, 1977) reported two Plinian eruptions at 24.5 and 11.6 Ka; García-Palomo et al. (2002) reported four Plinian eruptions at ~36, ~24.5, 12.1, and 10.5 Ka, dated from the corresponding debris flow avalanches. Aceves-Quezada et al. (2007) reported activity on 14 dates from 1.4 Ma to 3.3 Ka, including andesitic lava flows, debris flows and avalanches, lahars, pumice, and ash flows. Arce et al. (2003) described a Plinian eruption at 10.5 Ka.

The Plinian products and erupted bulk-rock compositions of NT show that the eruptions originated in an upper crustal reservoir (Arce et al., 2013a and b). Weber et al., (2020) concluded that a hybridization processes of deep basaltic-andesite recharge magma and an upper crustal silicic mush was reflected in the compositional zoning of all mineral phases; they concluded that NT is fed from two spatially separated magma sources residing either in the upper mantle or the lower crust.



a) **b)**

Figure: 1

Legend: Tmv basaltic lavas; Tmpv andesite-basaltic lava flows; Tpv basalt and andesite; Tpvc volcanic rocks and alluvial deposits; Qpvc lahars and volcanoclastic deposits; Qpla lacustrine sediments; Qpv basaltic lava flows; Qla lacustrine deposits and volcanic ash.

Fig. 1 a) Topography of the Nevado de Toluca area and location of two 3D inversions: the larger, black rectangle corresponds to the 1000 m resolution inversion, and the smaller black rectangle to the 500 m resolution. Also shown, are the locations of two cross-sections-oriented N-S and E-W (magenta) and obtained from the inverted voxel. b) Geologic map of Nevado de Toluca volcano corresponding to the area covered by the large rectangle. The larger red triangle shows the location Nevado de Toluca. The small red triangle W of NT corresponds to El Gordo volcano, whilst the one to the N corresponds to El Molcajete volcano. Lines in black represent geologic

faults: F1 (Tenango-San Antonio Fault System) and F2 (Taxco-Querétaro Fault System). Figure 1a made with GeoMapApp (www.geomapapp.org) / CC BY/ (Ryan et al., 2009). Figure 1b adapted from the Geologic Chart of the State of Mexico, https://ifomegem.edomex.gob.mx/carta_geologica.

Characterization of volcanic structures in terms of gravity varies depending on several factors. The resolution of the gravity used in the study is of fundamental importance; large scale studies involving hundreds of kilometers traditionally have used low-resolution data sets. The studies in the islands of Hawaii are an example (Kauahikaua et al., 2000), and in the Canary Islands (Camacho et al., 2018); in both instances positive anomalies were associated with portions of the volcanic region. In the case of Hawaii, positive anomalies are associated with dense cores, interpreted as magma storage regions, whilst in the case of Lanzarote, in the Canary Islands, three high-density regions are associated with three main volcanic complexes. In both cases, ground gravity surveys were used.

In inactive volcanic systems, whose activity ceased several Myr ago, the magma chambers, the intrusives, and the lava conduits have by now crystallized and cooled off, giving rise to anomalies with high density values, associated with positive Bouguer anomalies, and high susceptibility values. On the contrary, young, dynamic volcanoes fed by magma chambers with active mush and partial melts discharged through the conduits associated with their plumbing systems, usually present negative Bouguer anomalies, corresponding to the concentration of low-density materials, and lesser magnetic susceptibility values. Cases may occur in which both situations may appear, as in the case of Colima volcano (Guevara et al., 2021) or Kilauea volcano in Hawaii (Kauahikaua et al., 2000), in which old eruption paths have been abandoned and substituted by young, active plumbing systems.

METHODOLOGY

We obtain the gravity data from the GGMplus data set, discuss data resolution, and obtain the Bouguer anomaly in the study area. Two 3D inversions were produced with resolutions of 1000 and 500 m. The former corresponds to the larger rectangle shown in Figures 1a and 2, and the second (500 m resolution) encompasses the NT structure.

Data Processing

The GGMplus gravimetric data set was used for the 3D inversion (Hirt et al., 2013). This model presents the gravimetric data in two formats: as a FA anomaly and the gravity observed on the surface (G_{Obs}). The advantages of using the GGMplus model versus other high-resolution models is discussed in Camacho and Alvarez (2021). In this work, we calculated BA from G_{Obs} and this correction was included according to the new gravimetric standard of the USGS (e.g., Hildenbrand et al., 2002).

The theoretical gravity was obtained for each point of the data set (equation 1) (Wollard, 1979) calculate the BA, where the coefficients were: g_e=978032.67715 mGal, k=0.01931851353, and e^2=0.0066938002290. Coefficients k and e are dimensionless.

$$G_{teo} = g_e \frac{1 + k * (\sin \varphi)^2}{\sqrt{1 - e^2 (\sin \varphi)^2}} \quad (1)$$

The elevation at each point must be known; to accomplish this, we used the topographic model SRTM90 with a 7.5 arc-sec resolution which was the same as in the GGMplus model (Jarvis et al., 2008; https://srtm.csi.cgiar.org/srtmdata). Subsequently, the values of the ellipsoidal height (h_{ellip}) and the geoid height were placed at geoidal height (H_{geo}) through equation (2) (Li and Götze, 1996). For the following formulas the geoidal height (H_{geo}) will be defined as height (h).

$$h_{ellip} = H_{geo} + N \quad (2)$$

Where N is the geoid height, which can be readily observed in the page of ICGEM (Barthelmes & Kohler, 2016).

Knowing the height from the DEM at each point, we obtained the height correction (C_h) through equation (3).

$$C_h = \left((0.3087691 - 0.0004398 * sin(\varphi)^2)h + 7.2125 * 10^{-8}h^2\right)\left[\frac{mGals}{m}\right] \quad (3)$$

We then calculated the atmospheric correction (C_{atm}) considering the gravimetric attraction produced by the mass of air over the point determined with equation 4 (Hildenbrand et al., 2002).

$$C_{atm} = 0.874 - 9.9 * 10^{-5} * h + 3.56 * 10 * 10^{-9} * h^2 \quad (4)$$

The Bouguer correction ($C_{Boug_2^\circ}$) is the correction that eliminates the gravimetric attraction of the masses existing between the reference level and the point on a topographic surface (equation 5).

$$C_{Boug_2^\circ} = 2\pi * G * \rho * h * \left(\frac{\alpha}{2} - \eta * \left(1 + \frac{1}{2\alpha}\right)\right)\left[\frac{mGal}{m}\right] \quad (5)$$

Where α and η are coefficients defined by Lafehr (1991), G is the gravimetric constant, and ρ the density of the medium.

For the topographic correction (C_{topo}), we used the method implemented in the Oasis Montaj program of Geosoft, which uses the algorithm proposed by Kane (1962) and supplemented by Nagy (1966). AB was then calculated with equation (6).

$$AB = G_{Obs} - G_{teo} \pm C_{alt} \mp C_{Boug2^\circ} + C_{atm} + C_{topo} \quad (6)$$

The results produced the Bouguer anomaly map shown in Figure 2. The region was much larger than the area covered by the NT volcano to allow for additional modeling in various expanses of this region.

Data Resolution

The resolutions of the gravity and magnetic data sets are relevant when comparing the inversion results. Ideally, one would like to achieve the same high resolution in both data sets. However, aeromagnetic data with adequate resolutions are sometimes missing from study areas, as in the case of the NT region. The options were: i) not to invert the magnetic data or, ii) use a magnetic data set with a smaller resolution if available. In this case we opted for the latter, using the EMAG2V3 satellite data set and adding information to the results' interpretation. In every instance, we used the topographic model SRTM90 with a 7.5 arc-sec resolution, which was the same as in the GGMplus model.

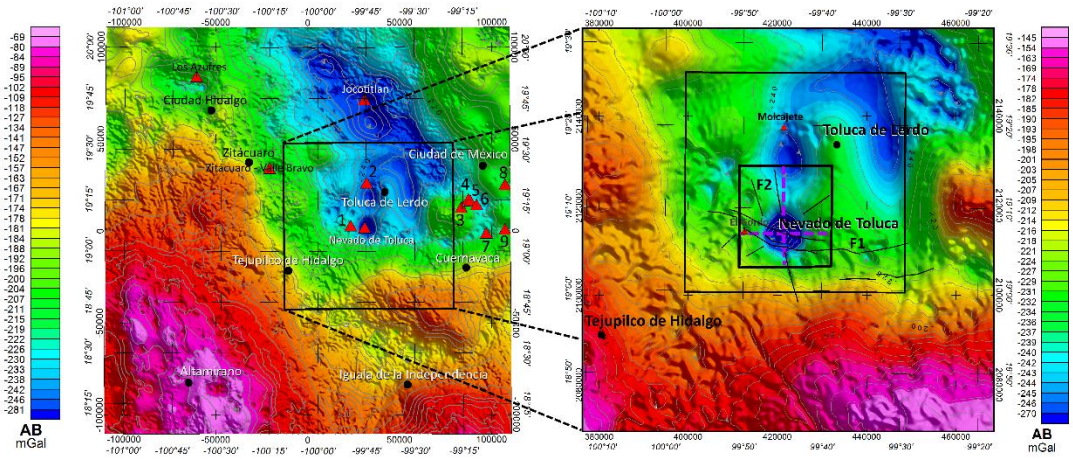
The EMAG2V3 is a global Earth Magnetic Anomaly Grid compiled from satellite, ship, and airborne magnetic measurements with a resolution of 2 arc-min (~3700 m) and an altitude of 4 km above the geoid (Meyer et al., 2017; Figure 3). The GGMplus gravimetric data set (Figure 2) with a resolution of 7.5 arc-sec (~220 m) was used here (Hirt et al., 2013); this model is available from http://ddfe.curtin.edu.au/gravitymodels/GGMplus/. Although the resolutions between the gravity and magnetic data sets were different, the results were complementary and useful for confirming tendencies in either data set, as will be disclosed later in the text.

The two available satellite gravity data sets of higher resolution were compared in a companion study (Camacho and Alvarez, 2021), and it was concluded that the GGMplus data set presently provides the highest resolution. They compared their frequency histograms, Free Air anomalies, power spectra, and simple Bouguer anomalies. The nature of the digital elevation models used for data reduction was also addressed. From a volcanic viewpoint, where the acquisition of gravity ground data is particularly difficult, and in the case of active structures, a task of high risk, having a satellite data set of the area represents a major advantage. Indeed, satellite determinations are distributed uniformly, whilst ground measurements are seldom obtained evenly on volcanoes. In addition, most satellite data sets are freely obtained through servers, and finally, satellite data sets also have a global coverage that makes their application suitable for any volcanic region in the world within the latitudinal limits of the satellite.

we want to stress the fact that the data resolution and the resolution of an inverted model are different. The latter refers to the size of the voxel units used to perform the inversion; further discussion of this topic is made in the 3D inversion section.

Bouguer Anomaly

We used a satellite-derived Bouguer anomaly data set, covering several times the area occupied by the NT structure, which corresponds to the GGMplus data set (Hirt et al., 2013). The idea of processing high-resolution data for the larger area, is to be prepared for the expansion of this analysis to neighboring regions. Gravimetry data were prepared for inversion through a Gaussian filter that separates the residual, in order to highlight the level structures associated with volcanic edifices.



a) **b)**

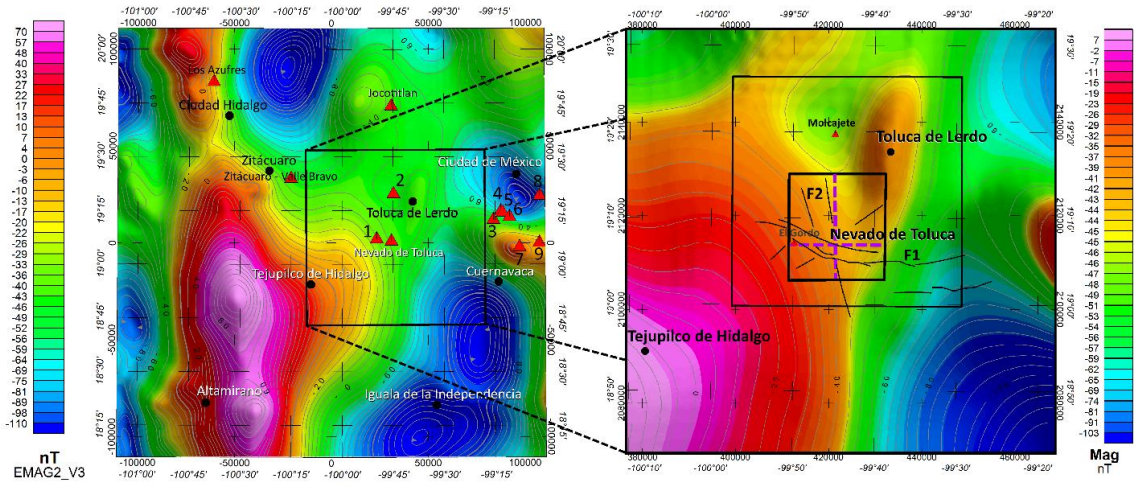
Figure: 2

Fig. 2 a) Complete Bouguer anomaly of the region surrounding the Nevado de Toluca (NT) volcano corresponding to the GGMplus model. Red triangles represent volcanoes: 1 El Gordo, 2 Molcajete, 3 Ajusco, 4 Xitle, 5 Cuautzontle, 6 Oloica, 7 Chichinautzin, 8 Tlaloc, 9 Xaltepec.

b) The black, larger rectangular polygon corresponds to the 1000 m resolution 3D inversion, and the smaller, black polygon to the 500 m resolution 3D inversion discussed ahead. The perpendicular, dashed magenta lines show the locations of the two sections trending N-S and E-W across the NT volcanic structure. F1 (Tenango-San Antonio Fault System) and F2 (Taxco-Querétaro Fault System) represent E-W and NNW-SSE trending fault systems through the volcano's structure (Torres-Orozco et al., 2017).

The Bouguer anomaly map (Figure 2) shows extended positive anomalies to the S and W of the NT volcano. An extended gravity low in the NE portion shows two trends. One is a SE-NW trend extending across the map in that direction; this major, SE-NW negative anomaly runs parallel to Sierra de Las Cruces consisting of an imbrication of volcanic edifices, lava flows, lahars, and pyroclastic deposits. The second, corresponding to the NT region, is located SW of the former and consists of a N-S, horseshoe-shaped anomaly whose western branch shows at its southern end the rounded, negative anomaly of NT. Two polygons (in black) enclose the NT area where the 3D gravity inversions were performed.

Negative gravity anomalies are often related to volcanic edifices associated with the presence of magma chambers and volcanic plumbing systems (e.g., Alvarez and Yutsis, 2015; Guevara et al., 2021; Alvarez and Camacho, 2023). The anomaly low associated with NT is circular and quite like the anomaly low immediately to the north; the difference is that the latter does not show an associated volcanic structure.



a) **b)**

Figure: 3

Fig. 3 a) Magnetic anomaly map of the region surrounding the Nevado de Toluca volcano corresponding to EMAG2 data with a resolution of 2 arc-min (~3700 m), reduced to the pole according to the standard procedure (Baranod & Naudy, 1964), I=46.58º, D=5.88º. Red triangles represent volcanoes: 1 El Gordo, 2 Molcajete, 3 Ajusco, 4 Xitle, 5 Cuautzontle, 6 Oloica, 7 Chichinautzin, 8 Tlaloc, 9 Xaltepec. b) Close up view of the magnetic anomaly around Nevado de Toluca volcano. The black, larger rectangular polygon corresponds to the 1000 m resolution 3D inversion, and the smaller, black polygon to the 500 m resolution 3D inversion discussed ahead. The perpendicular, dashed magenta lines show the locations of the two sections trending N-S and E-W across the NT volcanic structure. F1 (Tenango-San Antonio Fault System) and F2 (Taxco-Querétaro Fault System) represent E-W and NNW-SSE trending fault systems through the volcano's structure (Torres-Orozco et al., 2017).

The magnetic anomaly (Figure 3) was obtained from the satellite data set of EMAG2 (Meyer et al., 2017) with a resolution of 2 arc-min, and it was reduced to the pole. Owing to the difference in resolution with respect to that of the gravity data set, we used its 3D inversion to support the finer gravimetric results. We restricted the magnetic inversion to the smaller rectangle in **Figures 1** and **2**. The region of NT does not exhibit a distinctive magnetic anomaly, as in the case of the Bouguer anomaly; it is located between the two, dominating N-S highs in the magnetic map, showing some local disturbances.

RESULTS

3D Inversions

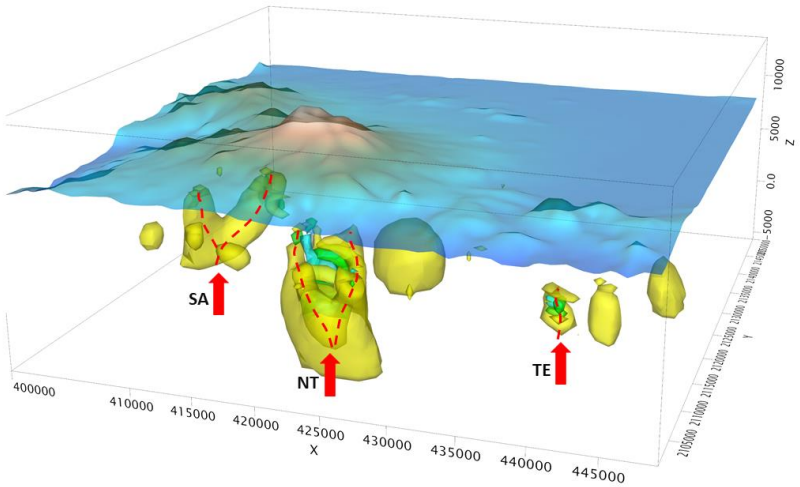
We performed the 3D gravity inversions using the method described by Macleod and Ellis (2013) based on the theoretical considerations of Ellis et al. (2012). The code was implemented in the Oasis Montaj program of Geosoft. The program uses a Cartesian Cut Cell algorithm (CCC) to represent geologic volumes and an Iterative Reweighting Inversion algorithm (IRI, Ingram et al., 2003) to match the observed results with the calculated ones within established error limits, that in these cases is 5% of the standard deviation. The inversion results are provided as densities in g/cm^3 when making a gravity inversion, and magnetic susceptibility (SI units) when

performing a magnetic inversion. The depth of the inverted volume was proportional to the size of the basic volume selected for the calculation. Typically, choosing cubes of 500-m-long edges will attain depths of 5-6 km and greater depths can be obtained at the expense of the resolution. When referring to resolution we must bear in mind that there is the high-resolution of the data used to obtain the Bouguer anomaly in Figure 2, in the gravity data case, and there is the resolution of the model proper. Models may have different dimensions; in this study we used models of dimensions in the X-Y plane of 1000 and 500 m, which we call the model resolution. To optimize computation, a subset of the high-resolution data set is used, selected according to the model resolution, to perform the inversion. An example appears ahead (Figure 5b) of the set of stations used for the inversion.

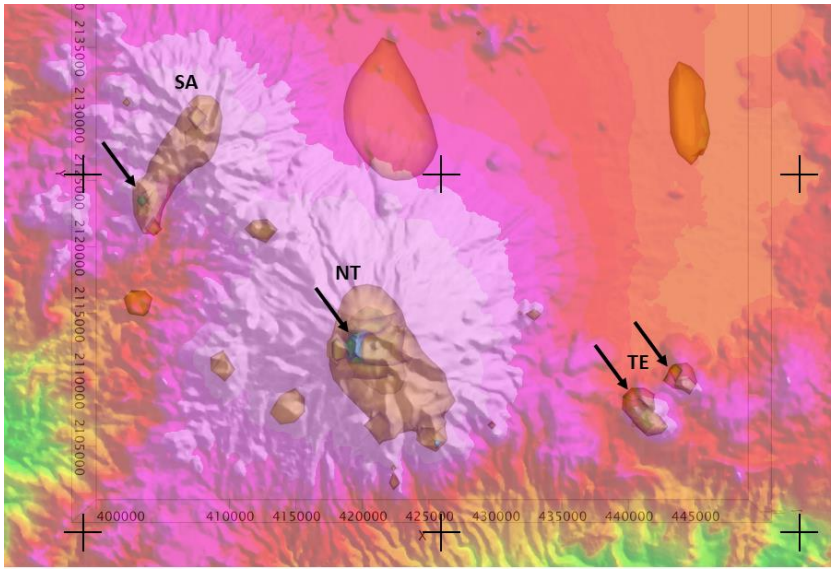
1000 m Resolution

The rectangle with the 1000 m resolution, the largest rectangle in Figures 1 and 2, was inverted first to learn about the volcanic sources in that area, before proceeding to the analysis of the NT structure. We performed the 3D inversion of the NT region in the 50 x 50 km area, as shown by the designated rectangles in Figures 1 and 2. In addition, the area included the San Antonio (SA) volcano in the NW of NT, and the Tenango (TE) region to the east containing fissure vent lava flows. From the density distribution obtained, we created geosurfaces, also called isosurfaces, to locate low-density regions. Figure 4a shows the geosurfaces enclosing regions with densities <2.56 g/cm^3 (yellow); these regions are associated with surface volcanic manifestations and are located directly underneath the volcanic structures or their manifestations (e.g., lava flows). The dashed, red lines indicate the possible trajectories of volcanic products towards the surface. The maximum depth of the inversion was -5000 m. The SA volcano is the oldest of the group; García-Palomo et al. (2000) assigned it a minimum age of 3.0±0.2 Ma, whilst suggesting that the volcano might have been formed as early as the Miocene. The yellow surface associated with SA (Figure 4a) bifurcates at an elevation of -830 m. The northern branch connects directly with the SA summit, indicating that it forms part of its plumbing system, whilst the southern branch outcrops 8 km SW of the SA summit (Figure 4b). Remarkably, both the yellow and green isosurfaces outcrop at that location. The peculiarity of this observation is that there are no clear associated volcanic structures, implying that the area should be studied in more detail. In contrast, the green surface does not outcrop at the summit of the SA volcano.

The golden surface under NT also shows a bifurcation close to the surface (Figure 4a), exhibiting a complicated pattern, and exposing the surface with a lower density (green) in the western portion of the summit (Figure 4b). Finally, a small deposit was identified as corresponding to the TE fissure-vent lava flows, apparently representing magma feeding through the TE fault system running E-W and reaching the NT volcano (García-Palomo et al, 2000). The green geosurface also outcrops at this location (Figure 4b). Other small, low-density regions will be discussed elsewhere.



a)

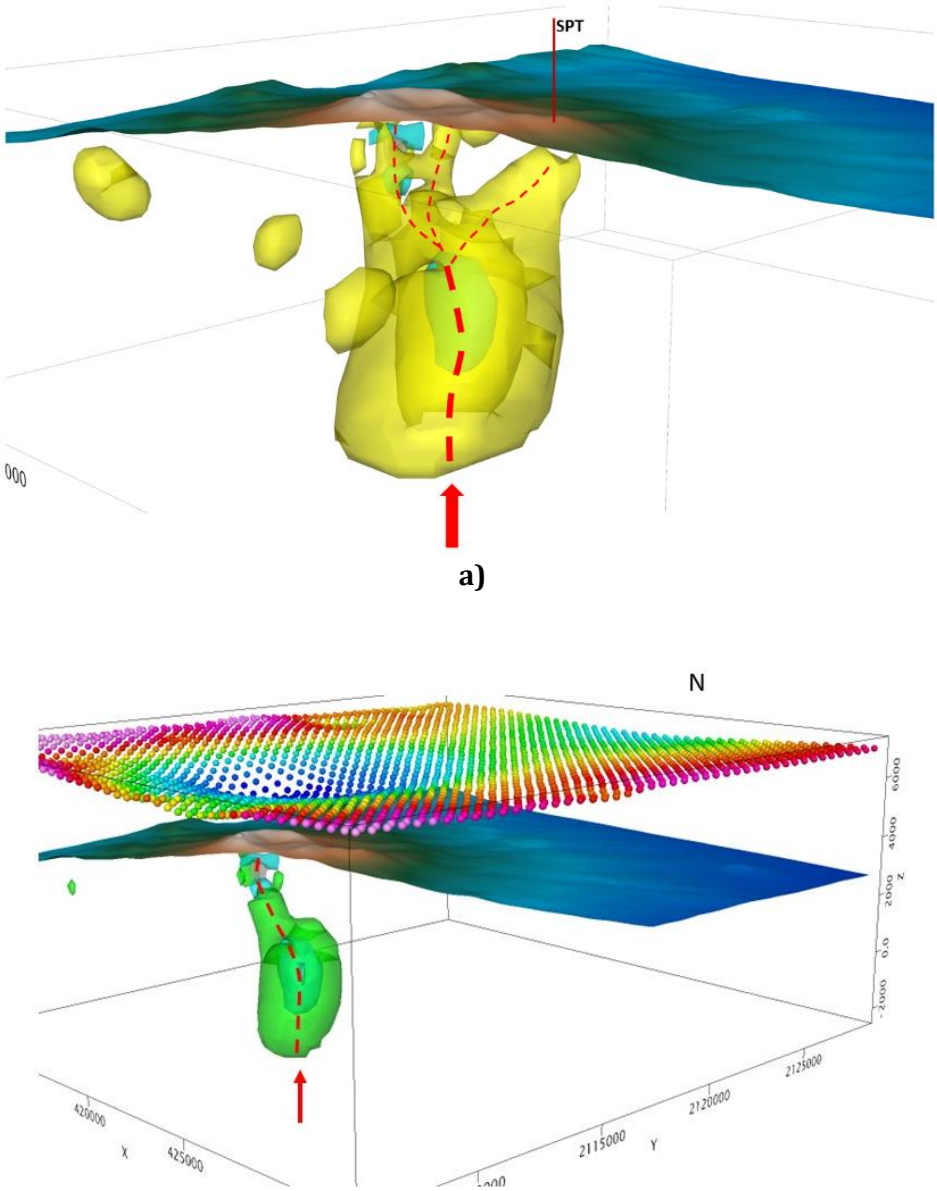


b)

Figure: 4

Fig. 4 Geosurfaces obtained from the 1000 m resolution 3D inversion superposed onto the local topography. a) The golden surfaces represent the regions whose densities are between 2.12 and 2.56 g/cm^3, and the green surfaces represent the regions with densities between 1.45 and 1.67 g/cm^3. The red arrows indicate the flow of volcanic products towards the upper chambers/conduits of each structure. The dashed red lines indicate the trajectories of flow inferred from these results. The digital elevation model is shown as a transparent layer to allow the visualization of the low-density surfaces; the colors in the map correspond to topographic ranges, also discernible in the topographic map of Figure 1. Owing to the 3d perspective, the geosurfaces appear displaced from their corresponding volcanic structures. b) Vertical view of the superposition of the geosurfaces and the topography; the arrows show the locations where the green isosurfaces outcrop. We restricted the discussion to the three locations identified as the San Antonio volcano (SA), Nevado de Toluca volcano (NT), and Tenango lava flows (TE).

The apparent displacement of the geosurfaces toward the south is corrected in the present view.



a)

b)

Figure: 5

Fig. 5 A closer view of the isosurfaces under NT obtained from the 3D inversion (Figure 4a) with a 1000 m resolution. Both figures extend vertically from the surface of NT volcano (+4600 m) to the bottom of the inversion (-2000 m). (a) An internal geosurface of lower density (blue) appears inside the translucent yellow one, corresponding to densities between 2.25 and 2.56 g/cm^3. San Pedro Tlanixco (SPT) corresponds to a monogenetic volcano at that location. b) By eliminating the outer, yellow layer close to the NT summit, a green geosurface is exposed, partially uncovering a gray one close to the surface, which we interpret as one of the exhaust

conduits of the volcano. The red arrow and dashed lines in a) and b) indicate the feeding and transport trajectories of volcanic materials. This geometry is inferred to represent the original plumbing system of the volcano. Both figures have the same depth and the same orientation; depth and north are indicated in Figure 5b. The colored dots on top of Figure 5b represent the location of the gravity stations selected to perform the 3D inversion; we note that this is a regularly distributed subset of the original, high-resolution data set. They are located on the surface of the ground, defined by the DEM reported above, and are selected by an algorithm of the program to optimize the inversion.

This preliminary analysis shows that low-density regions underlie the three main volcanic structures in the area. The inferred trajectories of volcanic materials from the interior to the surface are represented as red dashed lines in Figure 5. These geosurfaces present an onion-like structure, with the inner layers representing lower densities. We infer that volcanic activity at NT was initiated through the single western conduit shown in Figure 5b. The additional northern conduit shown in Figure 5a was subsequently activated where still another branch ending at SPT reaches the ground surface. We note that not all geosurfaces associated with surface volcanic manifestations contain the lowest density components (green and gray), perhaps indicating that they represent single expansion episodes of volcano-magmatic products. The lowest density trajectories should be the ones repeatedly used for the expulsion of such materials. According to Martínez-Serrano et al., (2004) volcanic activity at Nevado de Toluca (NT) volcano began 2.6 Ma ago with the emission of andesitic lavas; more recently (40 ka), eruptions have produced mainly lava flows and pyroclastic deposits of predominantly orthopyroxene–hornblende dacitic composition. One can assume that the andesitic lavas impregnated the conduits of the original plumbing system; whether the dacites modified the composition of the wall conduits cannot be ascertained in the present study.

500 m Resolution

Next, we performed the inversion of the Bouguer anomaly on the 500 m resolution (smaller rectangle in Figure 2). The 3D inversion displayed in Figure 6 shows a slice along the 65º azimuth to highlight the density characteristics under the NT volcano; this azimuth direction cuts across two vents and the central dacitic dome, called Ombligo (García-Palomo et al. 2002) The voxel was overlain by the corresponding digital elevation model of the structure for correlation purposes; it is shown displaced upwards to allow the density volume to be visualized. The major low-density anomaly is exposed, extending from the surface to the deepest portion of the model (-2000 m). However, the uppermost portion of the negative anomaly appears divided by a small high-density region, corresponding to the dacitic dome This region coincides with the highest portion of the volcanic structure.

The 3D magnetic inversion appears in Figure 7, also showing a slice of the inverted volume; a low-susceptibility zone corresponds to the low-density region of Figure 6. Since the magnetic model did not have the resolution of the density inversion, the results were not as accurate for defining near-surface details. The low-susceptibility region starts ~2 km below the surface and its shape appears to be circular, contrasting with the rectangular shape of the density anomaly. Both anomalies exhibit continuous increments of density/susceptibility when moving away from the anomalies.

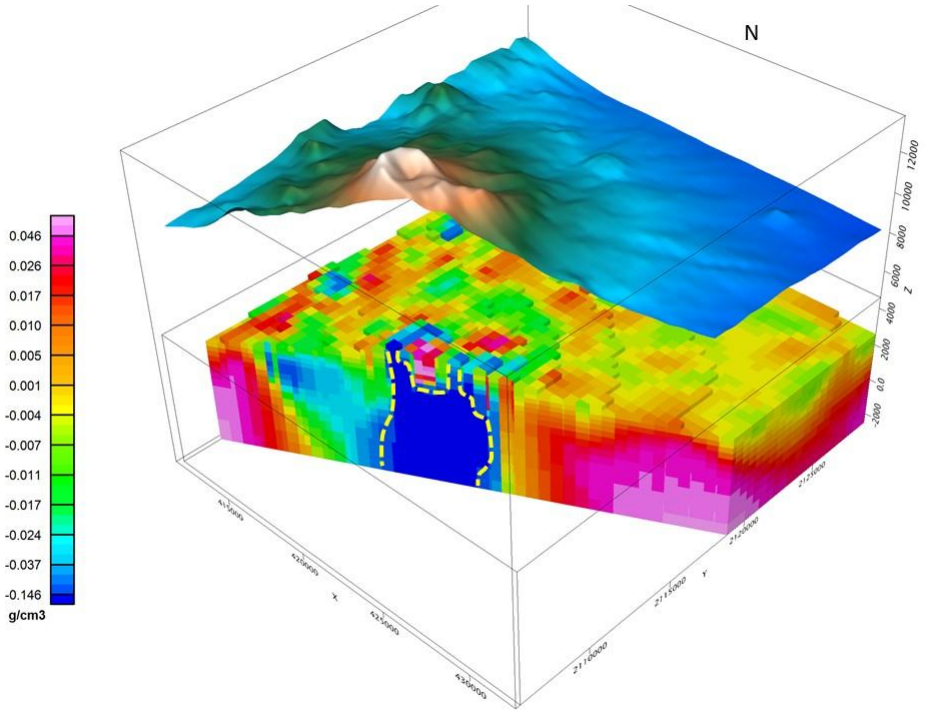


Figure: 6

Fig. 6 The 3D gravity inversion of the smaller rectangle in Figure 2, in the volume delimited by the lower box whose approximate dimensions are 25 x 25 x 5 km was performed; the resolution of the mesh is 500 m. The volume was cut along an azimuth of 65 degrees across the volcanic edifice to exhibit the low-density anomaly (blue) under the NT volcano. The upper box displays the digital elevation model associated with the volcano. The yellow dashed lines indicate the limits of the volcano's plumbing system; notice its bifurcation at the surface.

Low-density volcanic anomalies accompanied by regions of low susceptibility are likely to be associated with a magma chamber or its conduits; close to the surface they typically tend to reveal a single conduit or chimney (e.g., Tibaldi, 2015; Alvarez, 2017; Guevara et al., 2021) normally associated with the plumbing system of the volcano; notwithstanding, the case of the Hunga Tonga Hunga Ha'apai volcano exhibits a group of low-density regions on the surface of the volcano, instead of a single chimney (Alvarez and Camacho, 2023). In the case of NT, two conduits close to the surface are exposed; these were linked with different eruptive periods associated with cataclysmic eruptions (García-Palomo et al., 2002).

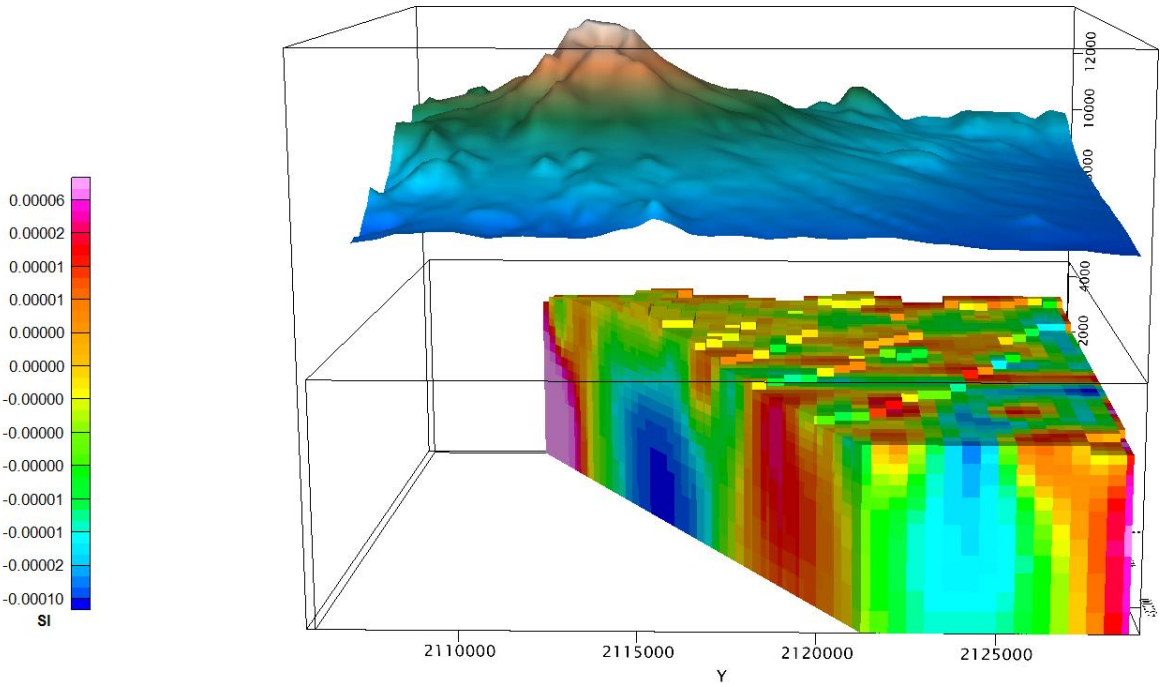


Figure: 7

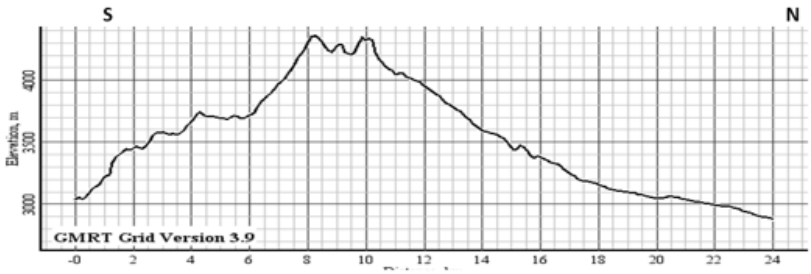
Fig. 7 3D magnetic inversion of the data in Figure 3 showing the magnetic susceptibility results, where the constant +1.0 x10^{-3} SI is to be added to the values in the scale. A low-susceptibility region is located directly under the summit of the NT volcano. Although the resolution of the magnetic data set is considerably lower than that of the gravity data set, their general trends agree.

NT Cross-Sections

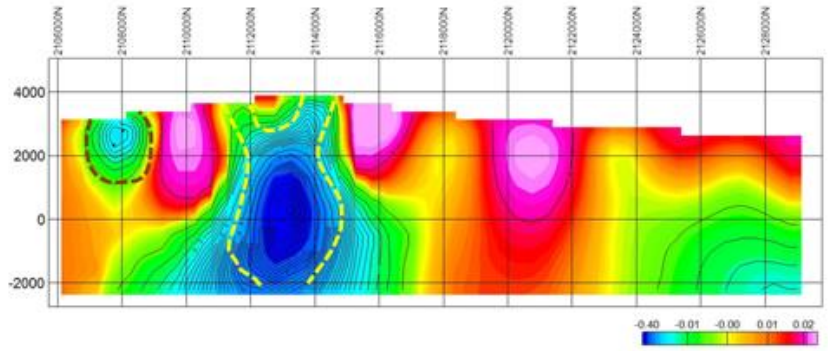
To further explore the characteristics of these inversions, we extracted cross-sections from the 500 m resolution voxels. Figure 8 shows the N-S cross-section of the density voxel along with a topographic profile of the structure, in which a split negative anomaly reaching the surface is observed, suggesting there are two exhaust conduits. To the east, a large positive anomaly constrains the negative one vertically, while a low-density anomaly flanks the anomaly to the west. The low-density anomaly continues vertically downwards from the limit of the inversion (i.e., below -2000 m). The split character of the anomaly reaching the surface is maintained in two additional cross-sections, as will be shown below.

The low-density anomaly associated with the volcanic structure shows that its near-surface portion is divided, suggesting that these exhaust vents were partially responsible for the repeated destruction of the crater and the eruptions of debris avalanches (Cantagrel et al., 1981; García- Palomo et al., 2000). The base of the anomaly appears extended towards the south. This anomaly also revealed that it has the lowest values at depths ranging from +1.5 to -1.0 km and we infer that this may be associated with the location of the volcano's magma chamber which fed by deeper sources of magmatic material. The appearance of a density minimum supports the existence of the chamber. Below elevations of 0 to +1 km, the low-density anomaly is double the size of the upper portion in this N-S projection. Models of the

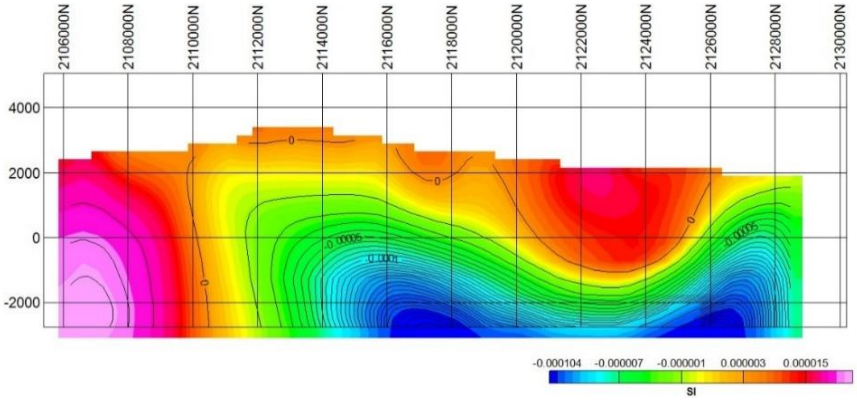
distribution of magma chambers in volcanoes usually locate several chambers distributed vertically in the crust (Magee et al., 2018; Cashman et al., 2017; Alvarez & Yutsis, 2015). Here, we only consider the uppermost chamber of the sequence at NT volcano.



a)



b)



c)

Figure: 8

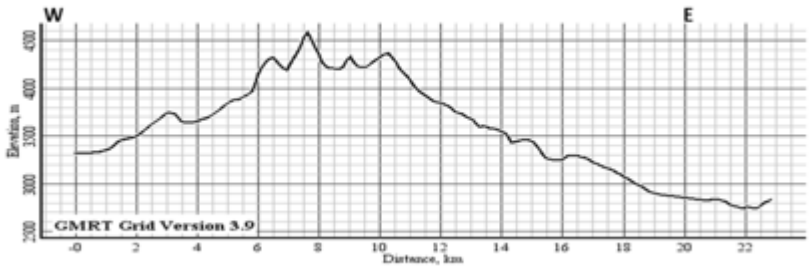
Fig. 8 Vertical cross-sections along the N-S line in Figure 2 showing: a) the corresponding topographic profile, b) the density anomaly associated with NT (contours are included to enhance the characteristics of the anomalies and the scale shows density increments (+) or decrements (-) over the reduction density of +2.67 g/cm^3, and c) the associated magnetic susceptibility (SI) cross-section, where the constant +1.0 x10^{-3} SI is to be added to the values in the scale. The terrain profiles of the cross-sections were averaged according to the elevation of

the voxel elements involved. Model resolution 500 m. Topographic profile extracted from GeoMapApp (www.geomapapp.org) 209 / CC BY / CC BY (Ryan et al., 2009)

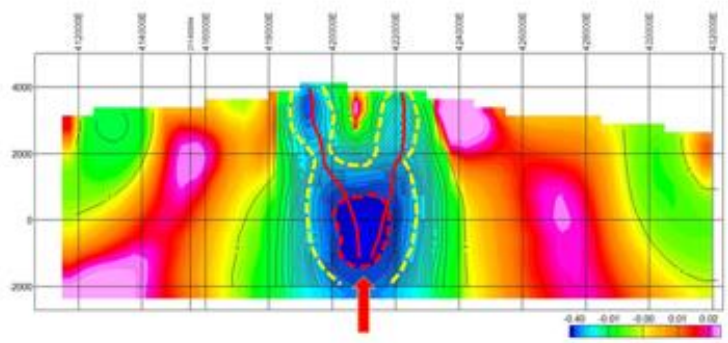
The N-S topographic profile is not symmetric (Figure 8a); it shows a bulge on the southern portion that is associated with the near-surface, low-density anomaly perched at the southern end of the line. It is worth noting that this local anomaly also shows a density minimum. The geometry of the main anomaly (Figure 8b) suggests that the perched anomaly is a result of magma injection directly from the lower portion of the main low-density anomaly.

The N-S cross-section resulting from the magnetic inversion corresponding to the magnetic susceptibilities is shown in Figure 8c. The cross-section displays a minimum value located to the north of the top of the volcanic structure, corresponding to a region where magnetization is minimal. Here, the two disconnected regions of minimum density shown in Figure 8b, one under NT and the other at the north end, appear connected at depths greater than the bottom depth (-2.5 km) of the inversion. Since low-susceptibility values are linked to temperatures near or above the Curie point, the probability of a deep, common magma feeder to the NT volcano and the associated region to the north is high. In the case of the volcanic structure, high-temperature materials have reached the surface, whilst in the anomaly to the north they seem to have been preserved at depth. The high-density region in the north portion of the profile (Between 2118000-2122000N) coincides with the high-susceptibility region (Figure 8c), indicating that this region functions as a local barrier to volcanic activity.

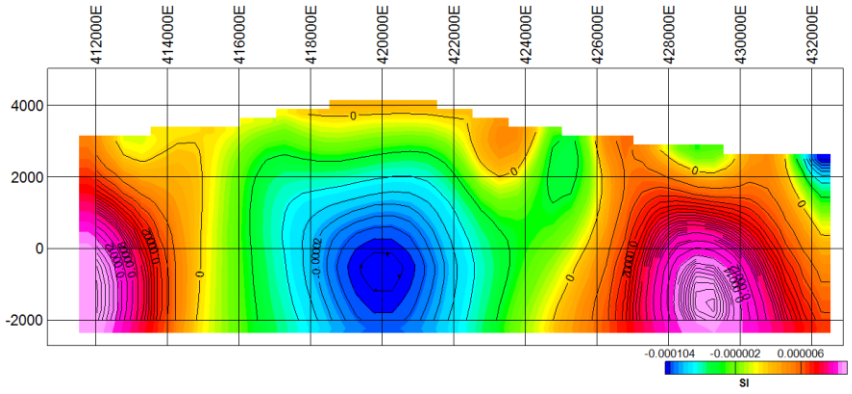
Figure 9 shows the E-W cross-section (Figure 2) across the crater of NT. The low-density anomaly associated with the volcanic structure most clearly shows the division in two of its uppermost volume. The extent of the anomaly at the surface is ~5 km across, including a central higher-density zone of ~1 km in diameter, and ~1.5 km deep. It clearly corresponds to the central dacitic dome called Ombligo which was emplaced between 10.5-9.0 ka (Aceves-Quezada et al., 2007). This higher-density zone exhibits different shapes in the two density cross-sections shown (N-S and E-W), either as the reason for, or a consequence of, the side deflection of the erupted materials. The crater has been described as having the form of a horseshoe (García-Palomo et al., 2002) since its eastern portion has been destroyed; this was likely associated with the magma ascent identified in Figure 9b which may have induced the explosive event. The identified magma chamber exhibits the same dimensions as those inferred for the N-S section, except that the bifurcation of the anomaly starts at the top of the proposed magmatic chamber. The center of the E-W anomaly is slightly deeper than the one appearing in the N-S cross-section (Figure 8b), highlighting structural differences in the central portion of the anomaly.



a)



b)



c)

Figure: 9

Fig. 9 Vertical cross-section along the E-W line of Figure 1 showing: a) the topographic profile, b) the density distribution associated with the NT volcano (the scale shows density increments of +2.67 g/cm^3); notice the dacitic dome represented by the high-density, vertical region between the two exhaust trajectories, suggested by continuous, thin red lines, and c) the magnetic susceptibility cross-section in SI units, where the constant +1.0 x10^{-3} SI is to be added to the values in the scale. The terrain profile of the cross-sections was averaged according to the elevation of the voxel elements involved; the contours are included to enhance the characteristics of the anomalies. Topographic profile extracted from GeoMapApp (www.geomapapp.org) 209 / CC BY / CC BY (Ryan et al., 2009)

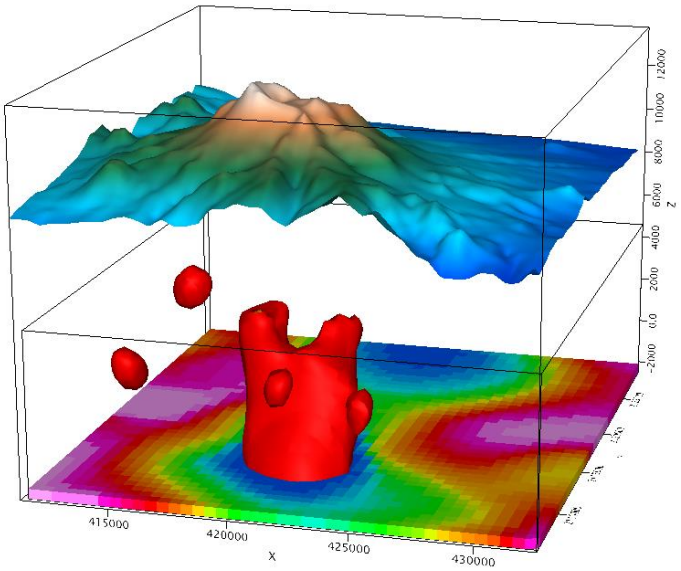
The repeated destruction of the crater summit seems to be directly related to the presence of the low-density anomalies near the surface. Of particular interest is the uppermost, low-density anomaly on the western side of the summit (Figure 9b). This anomaly contains a center which is absent in the corresponding anomaly on the eastern side of the summit, indicating the accumulation of low-density material in the form of a deposit with its center 500 m below the summit. This may constitute a potential hazard since it could give rise to a local flare up and we can only speculate that this type of activity could have contributed to some of the repeated destructions of the summit. The structural similarity with the perched anomaly in Figure 8b is worth mentioning.

The density and magnetic anomalies across the volcano's summit (Figures 8 and 9) show well-defined, coincident minima of density and magnetic susceptibility. Since the inversions were independent of each other, and involved different physical parameters, we considered this as a self-consistent system. We argue that the fact that we obtained minima in both physical properties indicates that this is a chamber in which material can be deposited. If it were just a conduit, we would not be observing minima of these properties. An accumulation of low-density, low-susceptibility (high-temperature) material could correspond to a mush at that location. We estimated the volume of this cylindrical reservoir as 15.9 km^3, considering a diameter of 2.2 km and a height of 4.2 km.

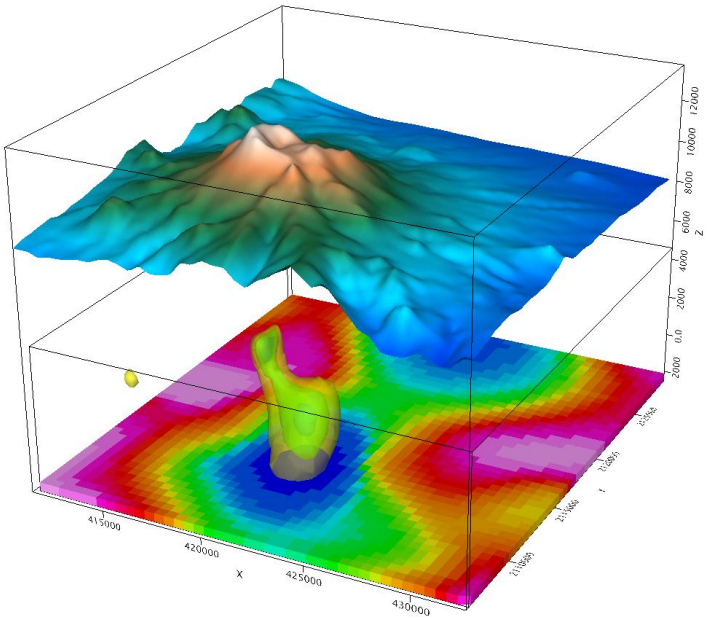
The inverted magnetic susceptibility (Figure 9c) exhibits a good correlation with the low-density zone. In particular, the regions of minimum density and minimum susceptibility coincide, reinforcing the notion that this may be the locus of the magma chamber of the NT volcano. Cantagrel et al. (1981) associated the abundant ash and pyroclastic flows with a shallow magma chamber. The distribution of the materials confining the low-density and low-susceptibility regions correspond to high-density and high-susceptibility zones, which also coincide in constraining them laterally (Figures 9b and 9c). Demagnetization can generally be explained by a change in mineral contents or by a rise in temperature. In the present case, we preferred the latter option, concluding that the regions of negative gravity anomalies are underlain by regions of low magnetic susceptibility.

Geosurfaces

The geosurfaces obtained from the 1000 m resolution inversion were refined from the 3D inversion with a 500 m resolution (Figure 4). The prominent red surface in Figure 10a corresponds to a density value of 1.784 g/cm^3, delimiting the larger densities outside the volume of this surface from the lower densities within it. This surface clearly shows the split character of the anomaly close to the surface, indicating that low-density material reaches the upper portion of the volcanic structure. The western and eastern sides of this anomaly reach the surface or close to it, whilst the middle portion remains ~2 km below. This surface was eliminated in Figure 10b, revealing surfaces with lower density values which we interpret to represent an older, initial stage of the volcanic plumbing system of the NT volcano. Like in many polygenetic volcanic structures, a single volcanic conduit formed during this earlier stage and located to the west of the summit is shown in Figure 10b. This suggests that a younger magmatic surge was responsible for the bifurcation of the volcanic conduits; one followed the earlier path and the other proceeded to the eastern side of the summit. The middle portion contains the Ombligo dome, as shown in Figure 8b. Further research may indicate whether the older and younger regions of magma ascent correspond to the two phases that built the NT structure, as suggested by Cantagrel et al. (1981).



a)



b)

Figure: 10

Fig. 10 a) Surface enclosing the region of lowest densities (red), obtained from the 3D inversion with a 500 m resolution shown in Figure 6, extending vertically from elevations of +4210 to -2200 m. The top of the surface clearly shows the shape of the bifurcation. b) When the red surface is removed, the lower densities are exposed, showing a single volcanic conduit to the west of the summit

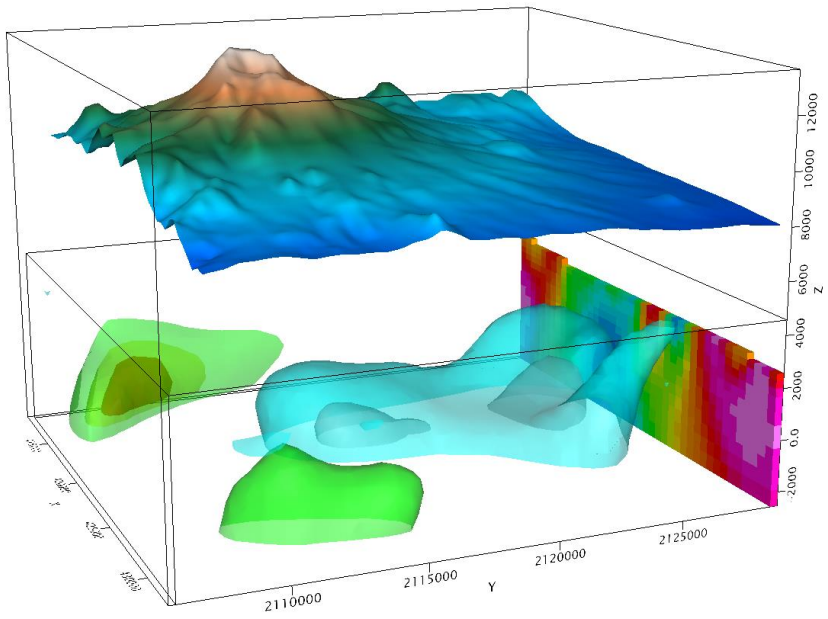


Figure: 11

Fig. 11 Magnetic geosurfaces obtained from the inversion in Figure 7; the Y-axis corresponds to the N-S direction. The blue iso-surface encloses magnetic susceptibilities ≤ -3.11 x 10^{-5} SI, and the green geosurfaces enclose values ≥ +12.0 x 10^{-5} SI; the constant +1.0 x10^{-3} SI is to be added to the values in the scale.

The volume distribution of the magnetic material shown in cross-section in Figure 8c can also be observed as a volume in Figure 11, where the low-susceptibility region (light blue) extends in the N-S direction, getting closer to the surface in the north of the region. Out of the two separate lower-density regions (gray) enclosed in this volume, the southern one is associated with the NT structure.

Volume Estimates

García-Palomo et al. (2002) reported on the oldest known materials ejected by the NT volcano which constitute the base upon which the volcanic edifice was built: 2.6 My-old light-gray porphyritic lava flows with a 100 m thickness, and 1.2-1.6 My-old primitive andesitic-dacitic lava flows with a 150 m thickness. The flows were overlain by a 200-m-thick stratigraphic column named the "Older Sequence" of the NT comprising interbedded debris flows, runout lahars, and minor lacustrine deposits. According to the geologic maps produced by Torres-Orozco et al. (2017) and Weber et al. (2020), we estimated the areal extent of the Old Nevado materials (2.6-1.2 Ma) to cover ~96 km^2. The combined thickness of the initial lava flows is 250 m, yielding an approximate volume of 24 km^3, which can be compared with the dimensions of the uppermost magma deposit identified in this work as ~15.9 km^3. To estimate volume recharge, we offer an illustration: We obtained a recharge volume of 2.4 km^3; assuming that this volume is only replenished 15% in each recharge, this process should have occurred around ten times during the initial stages of construction of the volcanic edifice, assuming that these volumes did not change significantly during that period. Deeper deposits must have

intermittently replenished this upper magma chamber, constituting the main portion of NT uppermost plumbing system.

CONCLUDING REMARKS

We found only one schematic description of the plumbing system of the NT volcano (Aceves-Quezada et al., 2007) in which a single chimney of the volcano was depicted, first during its early stages (Paleo-Nevado, about 1.4 Ma), and subsequently at the time of emplacement of the Ombligo dome between 10.5-9.0 ka. Neither stage showed the bifurcations of the upper plumbing system reported herein. The models presented here are based on the interpretation of the distributions of density and magnetic susceptibility of the rock formations constituting the volcanic edifice. They show that NT has a peculiar plumbing system, with two branches that surround, but do not completely enclose, the upper portions of the structure, conveying magmatic products to the volcano's summit. According to Figures 5 and 10, one can infer that the western branch is older than the eastern one, since there are no branches of lower density in the direction of the latter. Figure 8c shows the linking of a low-susceptibility region, below -2000 m, noting that in the same places, there are two independent gravimetric low-density anomalies separated by a region of high density that reaches the surface (Figure 8b). Figure 10a extends those results, showing that the low-susceptibility region has the shape of a deformed cylinder along the N-S direction; the northernmost portion rises towards the surface without reaching it. However, there is a group of volcanic edifices close to this region and along the N-S direction, some of which are clearly monogenetic and probably linked to this low-gravity and low-susceptibility anomaly. García-Palomo et al. (2000) reported that the latest deformation period in the region started during the late Pleistocene, ending in pure extension, and shifting $\sigma 3$ to a N-S direction; the authors noted that these faults appear to control the local, late Pleistocene to Holocene monogenetic volcanism. Their observations and ours complement each other, reinforcing the idea of these faults controlling the monogenetic volcanic activity in this region. Based on the cross-sections across the summit of the volcano (Figures 8 and 9) and their density and magnetic susceptibility distributions, we estimated the center of the magmatic chamber to be located between elevations of 0 and -1 km, or between 5 and 6 km below the NT volcano's summit. Based on considerations of geothermometry Arce et al., (2012) concluded that dacitic magma was stored at 5.8 to 7.7 km below the volcano summit. Given the uncertainties in both estimates, we consider they coincide within reasonable limits. Regarding the study of Weber et al., (2020) that based on their petrologic model observes that very mafic clino- and orthopyroxene compositions are present in the erupted products of NT, indicative of two deep, separated magma sources feeding the volcano, we can only comment that they must be the magma sources replenishing the shallower chamber modeled in this work. The high-resolution gravity analysis performed here on the structure of the NT volcano could be extended to practically any volcanic structure in the world's continents within ±60º latitudes where high-resolution GMMplus data is available, providing a powerful tool for analyzing volcanic formations.

ACKNOWLEDGMENTS

During the development of this work, MC received support from the Consejo Nacional de Ciencia y Tecnología (CONACYT, México). This study was supported by IIMAS, UNAM; we acknowledge material support from both institutions. This research did not receive any specific grant from funding agencies in the public, commercial, or not-for-profit sectors.

References

Aceves-Quezada JF, Martin del Pozzo AL, López-Blanco J (2007) Volcanic hazard zonation of the Nevado de Toluca volcano, central Mexico. *Nat Hazards*, 41: 159-180. Doi: 10.1007/s11069-006-9029-6

Alvarez R (2017) Mapping geologic interfaces that may alter seismic wave propagation in the Mexico City basin. *Geofísica Internacional*, 56-1: 37-56.
Doi: 10.19155/geofint.2017.056.1.4

Alvarez R, Yutsis V (2015) Southward migration of magmatic activity in the Colima Volcanic Complex, Mexico: an ongoing process. *Int. J. Geosciences*, 6: 1077–1099. https://doi.org/10.4236/ijg.2015.69085

Alvarez, R. and Camacho, M. (2023). Plumbing System of Hunga Tonga Hunga Ha'apai Volcano. Journal of Earth Science, 34(3): 706–716. https://doi.org/10.1007/s12583-022-1792-0

Arce JL, Macías JL, Vázquez-Selem L (2003) The 10.5 Ka Plinian eruption of Nevado de Toluca volcano, Mexico: stratigraphy and hazard implications. *Geol. Soc. Amer. Bull.* 115:230 – 248.

Arce, J. L., Layer, P. W., Lassiter, J. C., Benowitz, J. A., Macías, J. L., and Ramírez-Espinosa, J. (2013a). 40 Ar/39 Ar dating, geochemistry, and isotopic analyses of the quaternary Chichinautzin volcanic field, south of Mexico City: implications for timing, eruption rate, and distribution of volcanism. *Bull. Volcanol.* 75 (12), 774. doi:10.1007/s00445-013-0774-6

Arce JL, Gardner, and Macías, JL (2013b) pre-eruptive conditions of dacitic magma erupted during the 21.7 ka Plinian event at Nevado de Toluca volcano, Central Mexico. http://dx.doi.org/10.1016/j.jvolgeores.2012.09.012

Baranod, V., Naudy, H., (1964). Numerical calculation of the formula of reduction to the magnetic pole. *Geophysics*, 29, 67-79.

Bloomfield K (1974) The age and significance of the Tenango Basalt Central Mexico. *Bull. Volcanol*. 37: 585 – 595.

Bloomfield K (1975) A Late-Quaternary monogenetic volcano field in central Mexico. *Geol. Rundsch.* 64: 476 – 497.

Bloomfield K, Valastro S (1974) Late Pleistocene eruptive history of Nevado de Toluca, central Mexico. Geol. Soc. Am. Bulletin, 85: 901–906.

Baranod, V., Naudy, H., (1964). Numerical calculation of the formula of reduction to the magnetic pole. *Geophysics*, 29, 67-79.

Barthelmes, F., Kohler, W. (2016). International Centre for Global Earth Models (ICGEM), in: Drewes, H., Kuglitsch, F., Adam, J. et al., The Geodesists Handbook, 2016. *J. Geod.* 90 (10), 907–1205. https://doi.org/10.1007/s00190-016-0948-z.

Bloomfield K, Valastro S (1977) Late Quaternary tephrochronology of Nevado de Toluca, central Mexico: Institute of Geological Sciences, *Overseas Geol. Min. Res.* 46: 1–15.

Cashman, KV., Sparks, RSJ., Blundy, JD. (2017). Vertically extensive and unstable magmatic systems: A unified view of igneous processes. *Science* 355, eaag3055. DOI:10.1126/science. aag3055

Camacho M, Alvarez R (2020) Gravimetric analysis of the rifts and volcanic fields of the Jalisco block, Mexico. *Tectonophysics*, 791, 228577. https://doi.org/10.1016/j.tecto.2020.228577

Camacho M, Alvarez R (2021) Geophysical modeling with satellite gravity data: EIGEN-6C4 vs GGMplus. *Engineering*, 13, 690-706. https://doi.org/10.4236/eng.2021.1312050

Camacho, AG, Prieto, JF, Ancochea, E, Fernández, J. (2018) Deep volcanic morphology below Lanzarote, Canaries, from gravity inversion: new results for Timanfaya and implications. J. Volc. Geothermal Res., https://doi.org/10.1016/j.jvolgeores.2018.11.013

Cantagrel JM, Robin C, Vincent P (1981) Les grandes étapes d'évolution d'un volcan andésitique composite: example du Nevado de Toluca. Bull. Volcanol. 44: 177 – 188.

Capra L, & Macías JL (2000) Pleistocene cohesive debris flow at Nevado de Toluca volcano central Mexico. J Volcanol Geotherm Res 102: 149– 168.

DeCserna Z, Fries C Jr (1981). Resúmen de la geología de la hoja Taxco, Estado de Guerrero, México y Morelos, Mapa con texto explicativo, Carta Geológica. Hoja Taxco 14Q-h (7), Serie 1:100,000, No. 15. Instituto de Geología, UNAM.

Ellis RG, deWet B, Macleod IN (2012) Inversion of magnetic data for remnant and induced sources. Presented at the 2012 Australian Soc. Explor. Geophysicists (ASEG) 22nd Int Geophys Conf Exhibit, Brisbane, Australia, 26–29 February 2012.

Ferrari, L., Orozco-Esquivel, M.T., Manea, V., Manea, M., (2012), The dynamic history of the Trans-Mexican Volcanic Belt and the Mexico subduction zone, Tectonophysics, 522-553, 122-149.

García-Palomo, A., Macías, J.L., Arce, J.L., Espindola, J.M., (1996) Marco Geológico Estructural de la Región del Nevado de Toluca, Central México, Edo. de México. Actas INAGEQ 2, 115–120.

García-Palomo A, Macías JL, Garduño VH (2000) Miocene to Recent structural evolution of the Nevado de Toluca volcano region central Mexico. Tectonophysics, 318: 281– 302.

García-Palomo A, Macías JL, Arce JL, Capra L, Garduño VH, Espíndola JM (2002) Geology of Nevado de Toluca Volcano and surrounding areas, central Mexico. Geol. Soc. Am. Map and Chart Series MCH089, pp. 1– 48.

Guevara R, Yutsis V, Varley N, Almaguer J, Calderón-Moctezuma A, Guevara-Mansilla O (2021) Geophysical determination of the Jalisco and Michoacán blocks boundary along the Colima graben. J. South Am. Earth Sci. 109, 103208. https://doi.org/10.1016/j.jsames.2021.103208

Hildenbrand TG, Briesacher A, Flanagan G, Hinze, WJ (2002) Rationale and Operational Plan to Upgrade the US Gravity Database. USGS Open File Report, 1-12

Hirt C, Claessens S, Fecher T, Kuhn M, Pail R, Rexer M (2013) New ultrahigh-resolution picture of Earth's gravity field. *Geophys Res Let*, 40(16): 4279–4283. https://doi.org/10.1002/grl.50838

Ingram DM, Causon DM, Mingham CG (2003) Developments in Cartesian cut cell methods. Math Comp Simulation, 61 (3–6): 561–572.

Jarvis A, Reuter HI, Nelson A, Guevara E (2008) Hole-filled SRTM for the globe Version 4. Available from the CGIAR-CSI SRTM 90m Database. Available at: http://srtm.csi.cgiar.org/.

Kane MF (1962) A Comprehensive System of Terrain Corrections Using a Digital Computer. Geophysics, 27(4): 455-462. https://doi.org/10.1190/1.1439044

Kauahikaua, J., Hildenbrand, T.and Webring, M. (2000) Deep magmatic structures of Hawaiian volcanoes, imaged by three-dimensional gravity models. Geology 2000;28;883-886 doi: 10.1130/0091 7613(2000)28<883: DMSOHV>2.0.CO;2

Lafehr TR (1991) An exact solution for the gravity curvature (Bullard B) correction. *Geophysics*, 56(8):1179-1184. https://doi.org/10.1190/1.1443138

Li X, Götze HJ (1996) Topography and geoid effects on gravity anomalies in mountainous areas as inferred from the gravity field of the Central Andes. Phys Chem Earth, 21(4): 295–297. https://doi.org/10.1016/S0079-1946(97)00051-7

Macías JL, García-Palomo A, Arce JL, Siebe C, Espíndola JM, Komorowski JC, Scott KM (1997) Late Pleistocene–Holocene cataclysmic eruptions at Nevado de Toluca and Jocotitlán volcanoes, central Mexico. *In*: Kowallis, B.J. (Ed.), Proterozoic to Recent stratigraphy, tectonic and volcanology, Utah, Nevada, Southern Idaho and Central Mexico. Buffalo Y U Geology Studies, pp. 493–528.

Macleod IN, Ellis RG (2013) Magnetic vector inversion, a simple approach to the challenge of varying direction of rock magnetization. Presented at the 2013 Australian Society of Exploration Geophysicists–Petroleum Exploration Society of Australia (ASEG–PESA) 23rd International Geophysical Conference and Exhibition, 11–14 August 2013, Melbourne, Australia.

Magee, C., Stevenson, CTE., Ebmeier, SK., et al. (2018) Magma plumbing systems: a geophysical perspective. J. Petrology. 59-6: 1217-1251. doi: 10.1093/petrology/egy064

Martínez-Serrano RG, Schaaf P, Solís-Pichardo G, Hernández-Bernal MS, Hernández-Treviño T, Morales-Contreras JJ, Macías JL (2004) Sr, Nd and Pb isotope and geochemical data from the Quaternary Nevado de Toluca volcano, a source of recent adakitic magmatism, and the Tenango Volcanic Field, Mexico J Volc Geothermal Res. 138:77-110.

Meyer B, Saltus R, Chulliat A (2017) EMAG2v3: Earth Magnetic Anomaly Grid (2-arc-minute resolution). Version 3. NOAA National Centers for Environmental Information. https://doi.org/10.7289/V5H70CVX

Murcia H, Borrero C, Németh K (2019) Overview and plumbing system implications of monogenetic volcanism in the northermost Andes' volcanic province. J. Volcanol. Geothermal Res. 383: 77-87. https://doi.org/10.1016/j.jvolgeores.2018.06.013 0377-0273/.

Nagy D (1966) The Gravitational Attraction of a Right Rectangular Prism. *Geophysics*, 31(2): 362-371. https://doi.org/10.1190/1.1439779

Norini, G., Gropelli, G., Lagmay, A.M.F., Capra, L., 2006, Recent left-oblique slip faulting in central Trans-Mexican Volcanic Belt: seismic hazard and geodynamic implications, Tectonics, 25, TC4012, Doi:10.1029/2005TC001877

Ryan, WBF, Carbotte SM, Coplan J, O'Hara S, Melkonian A, Arko R, Weissel RA, Ferrini V, Goodwillie A, Nitsche F, Bonczkowski J, Zemsky R (2009) Global Multi-Resolution Topography (GMRT) synthesis data set, Geochem. Geophys. Geosyst, 10, Q03014, doi:10.1029/2008GC002332. Data doi: 10.1594/IEDA.0001000

Tibaldi A (2015) Structure of volcanic plumbing systems: A review of multiparametric effects. J. Volcanol Geothermal Res. 298: 85-135. https://doi.org/10.1016/j.jvolgeores.2015.03.023

Torres-Orozco R, Arce JL, Layer PW, Benowitz JA (2017) The Quaternary history of effusive volcanism of the Nevado de Toluca area, central Mexico. J South Am Earth Sci, 79:12-39. http://dx.doi.org/10.1016/j.jsames.2017.07.008

Weber, G., Caricchi, L., and Arce, J.L. (2020) The long-term life-cycle of Nevado de Toluca volcano (Mexico). *Front. Earth. Sci*. 8:563303. Doi:10.3389/feart.2020.563303

Wollard, G. P. (1979). New Gravity System - Changes in International Gravity Base Values and Anomaly Values. Geophysic*s*, 44(8): 1352-1366. https://doi.org/10.1190/1.1441012